XL CILAMCE
IBERO-LATIN AMERICAN CONGRESS ON COMPUTATIONAL METHODS IN ENGINEERING
NOVEMBER 11-14, 2019
Praiamar Natal Hotel & Convention
Natal, RN-BRAZIL

EXPERIMENTAL ANALYSIS OF A BEAM-COLUMN SUBJECTED TO NONCONSERVATIVE FORCES

Thiago José Duprat Fortes
Raul Rosas e Silva
Daniel Carlos Taissum Cardoso
tjdfortes@gmail.com
raul@puc-rio.br
dctcardoso@puc-rio.br
Departamento de Engenharia Civil e Ambiental - PUC-Rio
Rua Marquês de São Vicente, 225 - Gávea, RJ 22451-900, Brazil

Abstract. The structure known as Beck's Column consists of a beam-column, subject to a tangential follower force applied at its free end. Beck presented in 1952 the critical load, which induces the vibration of the structure (flutter). This paper uses a simple and general numerical model that allows the solution of the problem of columns with different properties and different boundary conditions associated to follower forces. In this work, emphasis was given to the experimental simulation of the phenomenon, in a qualitative way. A metal ruler was adopted to represent a slender fixed-free beam-column and, to simulate the following force, a brushless motor was attached to the free end. A thrust force is generated when air is moved by the propeller and the motor follows the rotation of the free end, changing the direction of the thrust force. Tests were performed with different setups in order to observe the effect caused in the presence of gravitational force (motor weight) in concomitance with the tensile and compression follower effect. The results were remarkably different, showing that the follower force can induce stabilization, flutter and divergence. As the analysis was qualitative, videos and photos were made to record the results. The values of critical loads and frequencies were within the range expected by numerical analysis. Attempts to instrument the tests with accelerometers and LVDTs (Linear Variable Differential Transformer) were made and a discussion is presented on the differences and influence of these devices on the structure behavior.

Keywords: Numerical Analysis, Rayleigh-Ritz, Enriched Functions

1 Introduction

In 1952, Von Max Beck studied a cantilevered column subjected to a tangential follower force at its free end, as shown in Figure 1, taken from [1]. Such forces are nonconservative and nondissipative. This structure, known as Beck's Column, is not an exact model of an actual structure, but just an idealized model.

Figure 1. Beck's Column, taken from [1].

Follower forces are mostly noted in structures subject to aerodynamic forces. The thrust generated by rockets in missiles and spacecraft are examples of follower forces [2]. Because of this, the study of these forces became a wide field in aerospace structures engineering.

Beck developed a dynamic criterion to determine the critical load of this problem. However, his results and related topics have not been appreciated well by structural engineers.

In 1961, when commenting on Beck's Column, Timoshenko and Gere stated that "no definite conclusion can be made (as yet) regarding the practical value of this result, since no method has been devised for applying a tangential follower force to a column during bending" [3].

In 1996, Koiter proposed the "elimination of the abstraction of the follower forces as external loads from the physical and engineering literature on elastic stability". "Beware of unrealistic follower forces", he concluded [4].

This paper presents a review of the analytical development for this problem and a numerical model to predict critical loads. The numerical model uses cubic polynomial functions enriched with sine functions combined with cubic polynomials (a generalized Fourier series), which do not interfere in the nodal displacements. This allows for simple treatment of follower nodal forces. In addition, it contributes with a set of experiments that illustrate the phenomenon of flutter. Hence, the contributions of the present study is to provide a new experimental approach to the modeling of the tangential forces in Beck's Column, and to demonstrate the capability of a simple and efficient numerical model to model the problem.

2 Literature Review

2.1 Numerical Anaysis

Beck's original study [1] stated that the original form of equilibrium is stable only up to a certain value of the tangential follower force, which he termed as critical load (P_{cr}). At a force exceeding this value, the structures do not present a new form of equilibrium, but a form of motion. For a cantilevered column, Beck concluded that

$$P_{cr} = 20.05 \, \frac{EI}{\ell^2}, \tag{1}$$

where EI represents the flexural rigidity of a beam in the plane of bending and ℓ is the column length.

It is well known that one of the basic differential equations for bending of beam-columns is

$$EI\,\frac{d^4y}{dx^4} + P\,\frac{d^2y}{dx^2} = q, \tag{2}$$

in which P is an axial compressive force and q is a distributed lateral load, as shown in Figure 2.

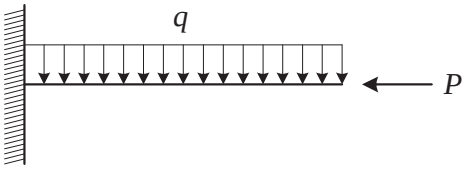

Figure 2. A beam-column.

When no lateral loads are applied, the differential equation reduces to

$$EI\,\frac{d^4y}{dx^4} + P\,\frac{d^2y}{dx^2} = 0. \tag{3}$$

Equation (3) can be rewritten as

$$\frac{d^4y}{dx^4} + k^2\,\frac{d^2y}{dx^2} = 0 \tag{4}$$

with

$$k^2 = \frac{P}{EI}. \tag{5}$$

The general solution to this differential equation is given as

$$y = A\,\sin(kx) + B\,\cos(kx) + C\,x + D, \tag{6}$$

where A, B, C and D are constants to be determined from boundary conditions.

When solving Beck's problem, Timoshenko and Gere [3] decomposed the force P into two components (P_1, in the vertical direction, parallel to column undeformed axis; and H, in the horizontal direction, perpendicular to column axis), as shown in Figure 3, taken from [3]. It can be noted that P_1 is approximately equal to P if deflections remain small.

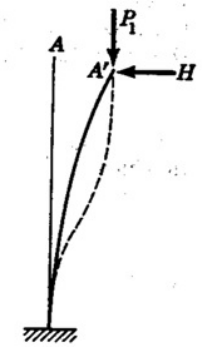

Figure 3. Timoshenko and Gere's decomposition.

The boundary conditions are

$$y = \frac{dy}{dx} = 0, \qquad \text{when} \quad x = 0$$

and

$$\frac{d^2y}{dx^2} = \frac{d^3y}{dx^3} = 0, \qquad \text{when} \quad x = \ell.$$

Applying these conditions to Eq. (6), it can be noted that a trivial solution with all constants null can be obtained. Therefore, Timoshenko and Gere reached a dead-end and concluded that, from a static point of view, only the straight form of equilibrium is possible within the elastic range.

So, Timoshenko and Gere approach the investigation of the stability of the column from a dynamic point of view, by assuming that the loaded column is subjected to an initial disturbance which produces small vibrations. They stated that "if these vibrations decrease with time, we can conclude that the straight form of equilibrium of the column is stable. (...) On the other hand, if the external forces acting on the column are such that the amplitude of the vibrations begins to grow without limit, the straight form of equilibrium of the column is unstable".

By applying D'Alembert's principle and substituting inertia forces for the lateral load on Eq. (2), he obtained the following:

$$EI\,\frac{\partial^4 y}{\partial x^4} + P\,\frac{\partial^2 y}{\partial x^2} + m\,\frac{\partial^2 y}{\partial t^2} = 0, \tag{7}$$

with m denoting the mass per unit length of the column.

Considering Eq. (5) and $a = m/EI$, and dividing by the flexural rigidity, the differential equation in (7) can be rewritten as

$$\frac{\partial^4 y}{\partial x^4} + k^2\,\frac{\partial^2 y}{\partial x^2} + a\,\frac{\partial^2 y}{\partial t^2} = 0. \tag{8}$$

The solution of this differential equation with constant coefficients can be taken in the form

$$y = A_0 f(x)\, e^{i\omega t}. \tag{9}$$

Substituting Eq. (9) into Eq. (8), the differential equation becomes

$$\frac{\partial^4 f(x)}{\partial x^4} + k^2\,\frac{\partial^2 f(x)}{\partial x^2} - a\,\omega^2 f(x) = 0, \tag{10}$$

for which the general solution is

$$f(x) = A\cosh(\lambda_1 x) + B\sinh(\lambda_1 x) + C\cos(\lambda_2 x) + D\sin(\lambda_2 x), \tag{11}$$

where

$$\lambda_1 = \sqrt{\sqrt{a\,\omega^2 + (k^4/4)} - (k^2/2)} \tag{12}$$

and

$$\lambda_2 = \sqrt{\sqrt{a\,\omega^2 + (k^4/4)} + (k^2/2)}. \tag{13}$$

In order to determine A, B, C and D, the four boundary conditions described previously for Timoshenko and Gere's solution must be adopted. Hence we now have four homogeneous equations for A, B, C and D. The undeformed straight column corresponds to zero values for the constants, as mentioned earlier. To obtain another solution, the determinant of the equations must be equal to zero, which leads to the following equation:

$$2a\omega^2 + k^4 + 2a\omega^2\cosh(\lambda_1\ell)\cos(\lambda_2\ell) + k^2\sqrt{a\omega^2}\sinh(\lambda_1\ell)\sin(\lambda_2\ell) = 0. \tag{14}$$

The angular frequency ω can be calculated for any value of P. Table 1 reproduces the first two frequencies (ω_1 and ω_2) obtained by Timoshenko and Gere for different P values, in a non-dimensional format.

Table 1. Frequencies of compressed column.

$\frac{P\ell^2}{\pi^2 EI}$	0	0.5	1.0	1.5	2.0	2.001
$\omega_1^2 \frac{a\ell^4}{\pi^4}$	0.125	0.26	0.30	0.46	0.96	0.98
$\omega_2^2 \frac{a\ell^4}{\pi^4}$	4.86	4.2	3.3	2.6	1.02	0.99

The values of ω_1^2 and ω_2^2 approach each other as P increases. Timoshenko and Gere conclude their solution for Beck's Column critical load stating that a more refined calculation shows that

$$P_{cr} = 2.008\,\frac{\pi^2 EI}{\ell^2} = 19.82\,\frac{EI}{\ell^2}. \tag{15}$$

Therefore, Timoshenko and Gere's solution presents a slightly lower value for the critical load (P_{cr}) when compared to Beck's original value (approximately 1,16% lower).

3 Numerical modeling

The analytical solution of columns with varying properties and different boundary conditions associated with follower forces is cumbersome. So, a simple and general numerical model was developed [5], using a Ritz approach with displacement functions to generate mass, elastic stiffness and geometric stiffness matrices for the modeling of the beam, including the load behavior in the so-called load stiffness matrix associated with the free end translation and rotation. The load stiffness matrix is symmetric in the case of conservative forces and non-symmetric for non-conservative forces.

As indicated in Eq. (16), the usual cubic polynomials for Euler-Bernoulli beam theory were adopted as functions associated with nodal displacements [6] (see Figure 4).

$$\mathbf{w_p}(x,L) = \begin{pmatrix} 1 - 3\frac{x^2}{L^2} + 2\frac{x^3}{L^3} \\ x - 2\frac{x^2}{L} + \frac{x^3}{L^2} \\ 3\frac{x^2}{L^2} - 2\frac{x^3}{L^3} \\ -\frac{x^2}{L} + \frac{x^3}{L^2} \end{pmatrix}. \tag{16}$$

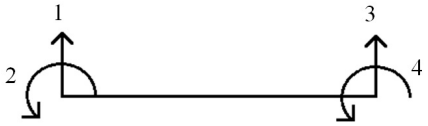

Figure 4. Nodal displacements.

In order to enrich the displacement field along the beam, it was added a series of functions which combine cubic polynomials and a sine function. These additional functions are constrained to have zero values for displacements and rotations at the beam ends. This allows for a simple procedure for treating different boundary conditions and refinement of solutions (N is the number of additional functions).

$$\mathbf{w_t}(x,n,L) = -\frac{n\pi}{L}x + \frac{n\pi}{L^2}\left[2+(-1)^n\right]x^2 - \frac{n\pi}{L^3}\left[1+(-1)^n\right]x^3 + \sin\left(\frac{n\pi x}{L}\right)\ ; \quad n = 1,\ldots,N. \tag{17}$$

The resulting matrices have dimensions $(N+4)\times(N+4)$, and are obtained in the usual way in Ritz analysis (finite element format with global conventional and additional functions forming a vector

$\mathbf{w}$). In the equations below, m is the mass per unit length of the beam, EI is the flexural rigidity of the beam cross section, P is the axial force along the beam, and L is the beam length.

$$\mathbf{M} = \int_0^L m\mathbf{w}\mathbf{w}^T dx. \tag{18}$$

$$\mathbf{K} = \int_0^L EI\mathbf{w}''\mathbf{w}''^T dx. \tag{19}$$

$$\mathbf{K}_g = \int_0^L P\mathbf{w}'\mathbf{w}'^T dx. \tag{20}$$

In the case of forces applied at the nodes, the load stiffness matrix $\mathbf{K}_L$ affects only the nodal functions. For the nodal displacements shown in Figure 4, consider the left end fixed and a tension force P applied at the right end of the beam. If it remains tangential to the beam upon rotation q_4 at the end, a transverse component appears, with the value Pq_4 (considering small rotations approximation). Hence, the corresponding "load stiffness" coefficient is $-Pq_4$. It results in the submatrix below, to be added to the adequate positions in the geometric stiffness. It should be remarked that all terms associated with enrichment functions are null.

$$\mathbf{K}_L = P \begin{pmatrix} 0 & 0 & 0 & 0 \\ 0 & 0 & 0 & 0 \\ 0 & 0 & 0 & -1 \\ 0 & 0 & 0 & 0 \end{pmatrix}. \tag{21}$$

The dynamical equations for the beam subjected to an initially axial force, disregarding damping, are

$$\mathbf{K}\mathbf{q} + (\mathbf{K}_G + \mathbf{K}_L)\mathbf{q} + \mathbf{M}\ddot{\mathbf{q}} = 0. \tag{22}$$

Assuming modes of vibration in the form $\mathbf{q} = \mathbf{q}_k \sin(\omega_k t)$, we are led to the following generalized eigenvalue problem expression for the calculation of the angular frequencies

$$\left[\mathbf{K} + (\mathbf{K}_G + \mathbf{K}_L) - \omega^2\mathbf{M}\right]\mathbf{q} = 0. \tag{23}$$

The resulting frequencies are affected by the magnitude of the load P. For divergence instability, the critical load corresponds to a zero frequency (see Figure 5). This case can be investigated statically by finding the smallest load magnitude which corresponds to a zero determinant of the tangent stiffness matrix (alternatively, and more efficiently, the first zero pivot in a Gauss decomposition, as shown in Figure 6). On the other hand, for flutter instability, the critical load corresponds to the coalescence of the two first frequencies, as shown in Figure 7. The approximated results f_1, f_2, f_3, etc.., are obtained by successive linear extrapolation and incremental analysis with increasing load and a bisection or similar procedure, as illustrated in figures 5, 6 and 7.

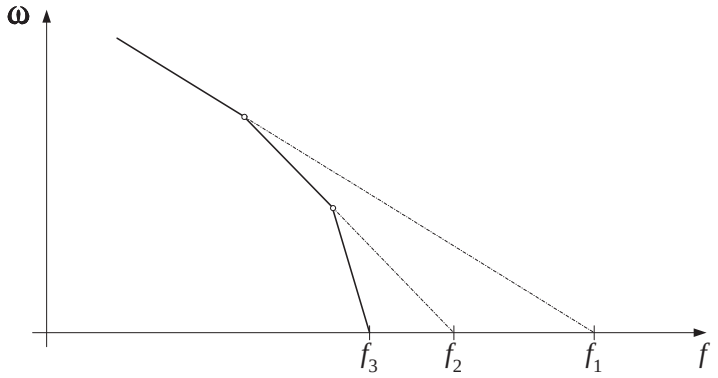

Figure 5. Static case (zero frequency at critical load).

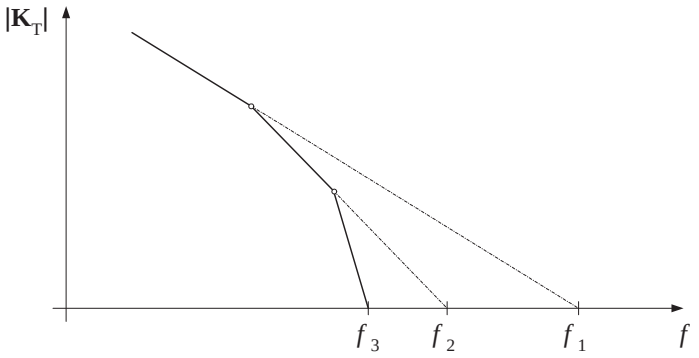

Figure 6. Static case (zero determinant and zero pivot at critical load).

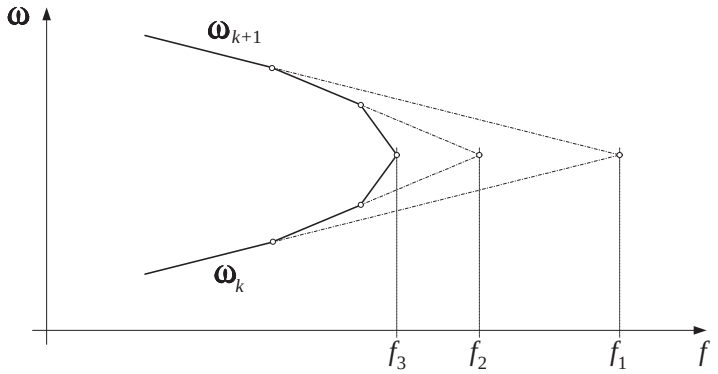

Figure 7. Dynamic case, showing the coalescence of two frequencies.

4 Experimental investigation

As commented in the previous section, applying a follower force in an experimental simulation is not an easy task. The column has to be subjected to a force that changes its direction with time. In this work, a force exerted by the thrust of a rotating propeller attached to the free end was used to simulate the follower force.

4.1 Material characterization

Determining the Young's Modulus of the material is important because with this determination it is possible to predict the force required for the material to reach the conditions predicted by Beck.

The critical static buckling load (P_{crs}) is calculated from the expression

$$P_{crs} = \frac{\pi^2 EI}{L^2}, \tag{24}$$

where L is the effective buckling length. In the case of the fixed-free pillar, the buckling length must be taken equal to 2ℓ.

Therefore, the ratio between the Beck's critical dynamic load (P_{crd}), presented previously, and the static critical buckling load (P_{crs}) is

$$\frac{P_{crd}}{P_{crs}} = \frac{\frac{20.05EI}{\ell^2}}{\frac{\pi^2 EI}{4\ell^2}} = 8.13. \tag{25}$$

The problem is that, when conducting an experimental analysis of such structure, buckling due to its own weight is easily achieved, whereas the conditions provided by Beck require more thrust.

To determine the Young's Modulus of the material, a direct tensile test was chosen. The ruler was cut in its half and, therefore, two specimens of 50 cm each were tested. In order for the ruler to be pulled by the MTS© High-Force Servohydraulic Test System, an adaptation was necessary: four metal plates were fixed on each test piece. It should be noted that the displacement control was set to a rate of 0.5 mm/min.

To measure the strain during test, a single strain gage was installed in the middle of each specimen. In order to attach the strain gage to the ruler, it was necessary to sand the surface of the ruler to make it smooth and adherent, since the numbers and the millimeter indicators had low relief.

Both specimens failed with rupture in the middle, where the strain gage was fixed. It is believed that this is due to the previous sanding process, which slightly decreased the straight section in that region.

The direct tensile test generated a stress vs. strain curve, in which it is possible to determine the Young's Modulus by verifying the slope of the line still in the elastic regime.

The stress vs. strain curve obtained as a result of the direct tensile test of the first test piece is shown Figure 8. The rupture stress was equivalent to 784.5 MPa.

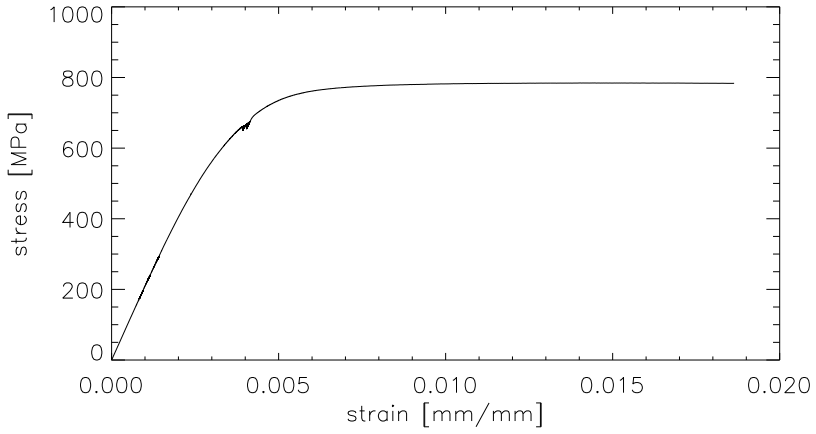

Figure 8. Stress vs. strain curve of the first test piece.

The stress vs. strain curve of the second test is shown in Figure 9. This time, the rupture stress was equivalent to 775.9 MPa.

In both experiments, it was found, by extracting the slope of the line in the elastic regime from each curve, that the Young's modulus was approximately 210 GPa, which was the value used in the calculations and in the qualitative comparisons.

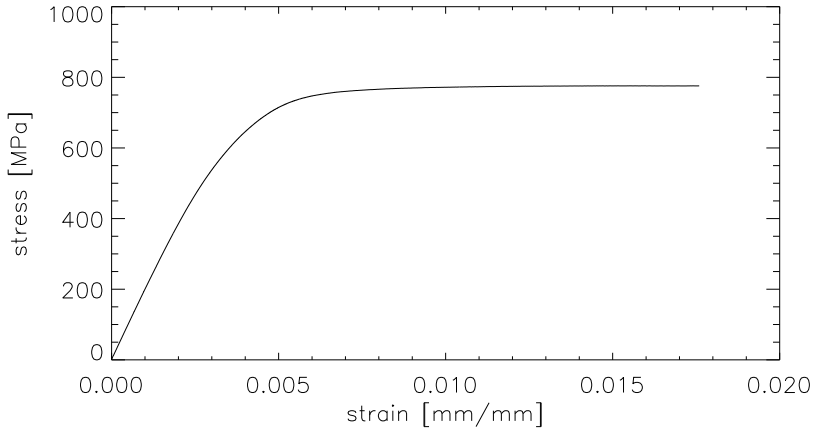

Figure 9. Stress vs. strain curve of the second test piece.

4.2 Brushless motor

It was decided to fix a brushless motor on the top of the metal ruler, simulating the slender column. This equipment is commonly used as a drone component. A thrust force was generated by the motor as the air is moved by the propeller. The motor axis (and the thrust force direction) rotates together with the rotation of the ruler at the end.

A major advantage of this type of motor is that, just by switching two wire connection to the motor controller, the motor will rotate in the opposite direction. Therefore, compressive follower forces (throwing air in the opposite direction of the ruler) and even tensile follower forces (throwing air in the direction of the ruler) were extremely easy to achieve.

Thrust test

To find out the maximum thrust generated by a given brushless motor, a test was performed in a Turnigy© thrust stand, in which different configurations were simulated so that the determined P_{cr} was reached. This stand has one degree of freedom and the thrust generated by the brushless motor causes a displacement that is measured by the apparatus. It is also possible to control the amount of energy driven into the motor, therefore changing its rotation speed. Different motors, propellers and batteries were used. The highest thrust, (slightly) higher than 11 N, was obtained with the Turnigy© aerodrive motor (model SK2830-750), a Turnigy© ten-inch diameter propeller with four-inch pitch and a MaxAmps.com© Lithium-Polymer four-cell (4S) battery, with 4000 mAh. After the thrust test in the stand, it was used an HJ© Digital Servo Tester to control the amount of energy driven into the motor, by generating a Pulse Position Modulation (PPM) signal for the motor controller.

4.3 Tests without attached instrumentation

It was decided to carry out tests without any attached instrumentation. It was also decided to submit the ruler to the follower forces of compression and tension. To capture its behavior, audio visual equipment was used, which resulted in photos and videos with a high frame rate per second.

Vertical in compression

The first simulation was performed by positioning the ruler vertically and applying a compressive force.

The main difficulty in this case was to position the cables that connect the battery to the motor without influencing the behavior of the ruler. It was not possible to extend the cables between the motor

controller and the motor, because this extension would affect the operation of the motor, since in this case the digital signals generated by the motor controller would not reach to the motor correctly. Because of this, the motor controller had to remain close to the brushless motor. Therefore, the cables between the battery and the motor controller were extended.

The ruler was positioned vertically. In order for it to remain vertical prior to the application of the compression follower force, the ruler was tied to the supports using thin light wires. After the motor was started, these wires were cut.

Despite having a slight inclination on one side, the structure did not collapse while the motor was on, generating the compression follower force. It is believed that this inclination is due to the different interferences present in the configuration, such as the presence of the motor controller near the motor, the cable arrangement and the mass of the motor/propeller assembly. It remained in this position until the motor was turned off, when the weights of the system caused the structure to buckle and collapse. So, it is easy to assume that the compressive follower force was responsible for avoiding the collapse.

Vertical in tension

The same configuration of the previous test was repeated, but this time the ruler was subjected to a tensile follower force. As mentioned before, in order to make the motor to generate the tensile follower force, it is sufficient to perform the inversion of two of the three wires coming out of the motor controller towards the motor. In this way, the wave generated by the motor controller is changed and the motor rotation is reversed, pushing the air in the opposite direction.

This time the structure did buckle. From the moment of the cutting of the support lines, the structure was directed to one side and, as the following force was increased, the structure curvature increased.

These two first tests were considerably conclusive in the qualitative analysis of the difference in behavior of slender columns when subjected to compressive and tensile follower forces. While in the first the compression follower force prevented the structure to buckle, in the second the tensile follower force contributed to the structure to buckle.

Upside down vertical in compression

After the first two tests, it was decided to perform the same tests, but with the ruler hanging upside down. In this way, the fixed end was positioned at the top of the ruler and the motor at the base. The main difference obtained in this case is that the structure is initially stable. In the previous configuration, the structure was statically unstable in the straight position (due to its slenderness and the weight of the equipment), and it was necessary to use lines to tie the ruler to the supports.

In the compression test, the structure presented a behavior similar to flutter instability and also reached the second mode of vibration.

Upside down vertical in tension

When subjected to a tensile follower force, the structure, which was statically stable prior to the motor start, became unstable. The follower force generated by the motor counterbalanced the stabilizing effect of the motor's weight, causing the structure to move like a pendulum.

Therefore, it was possible to conclude that the tensile follower force was able to destabilize a structure that appears to be initially stable.

Horizontal in compression

The vertical tests showed a considerable influence of the weight of the motor/propeller assembly. In order to reduce the effect of the weight, other tests were conducted with the ruler positioned horizontally. In this way, the displacement of the ruler would be in the horizontal plane, eliminating, therefore, the influence of the weight of the structure and its components, while still maintaining the effect of their masses in the dynamic behavior of the structure.

It must be said that the ruler has a little more than one meter and, in the previous tests, was being fixed only in the small flap that exists in one of the ends of it. For the horizontal test, however, it was necessary to fix a larger length of the ruler in the fixed end, since the moment generated by the weight of the motor/propeller assembly was non-negligible and the pressure exerted by the bench vise on the flap fixed was not sufficient to prevent rotation of the structure. Because of this, it was decided to set a further 10 cm (beyond the initial flap) and, therefore, in the horizontal tests, the ruler had a free length equivalent to 90 cm.

Of course, when the ruler size was decreased, it was necessary to calculate a new P_{cr}, for ℓ=900 mm. Thus, considering Eq. (1),

$$P_{cr} = \frac{20.05 \times 210 \times 2.1577}{900^2} = 0.011216 \text{ kN} = 11.216 \text{ N}. \tag{26}$$

Therefore, the motor thrust, measured at the stand, is very close to the new P_{cr} value.

For the horizontal in compression test it was also decided not to fix the cables and the motor controller to the ruler. In this configuration, these components were hanged, so that it was possible to observe the behavior of the ruler with less interference of them.

In this test, it was possible to observe that the ruler reached flutter instability and vibrated in the first, the second and even in the third vibration mode (see figures 10 and 11). This observation was made with naked eye and captured in video and photo.

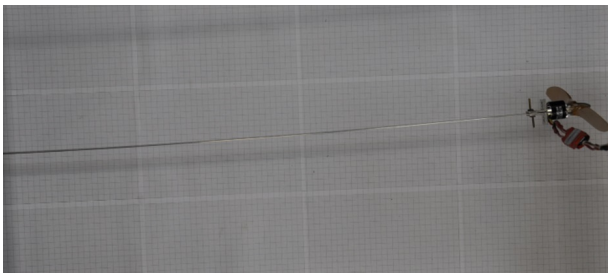

Figure 10. The structure, before the beginning of the test.

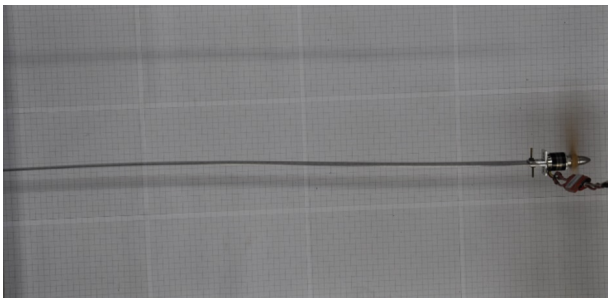

Figure 11. The structure, while the test was being conducted, reaching the second mode of vibration.

It was also observed that the mass of the motor remained almost at the same point, as shown in Figure 12. So, it is possible to conclude that existence of the motor in the structure interfered on its behavior when vibrating, being not quite similar to the vibration behavior of a fixed-free beam-column.

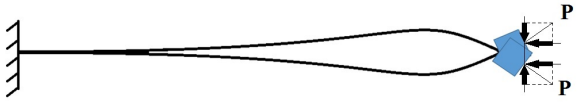

Figure 12. While vibrating, the mass of the motor remained almost at the same point.

Horizontal in tension

For the horizontal in tension test, the rotation of the motor was inverted. In addition, it was necessary to fix the cables and the motor controller back on the ruler. It was not possible that they remained hanging because, unlike observed in the "Horizontal in Compression" test, the tensile force destabilized the structure and, therefore, the position of the end of the rule (where the motor was installed) varies according to the increase of the tensile follower force. As in the "Vertical in Tension" test, as the following force increased, the structure's curvature also increased (see Figure 13).

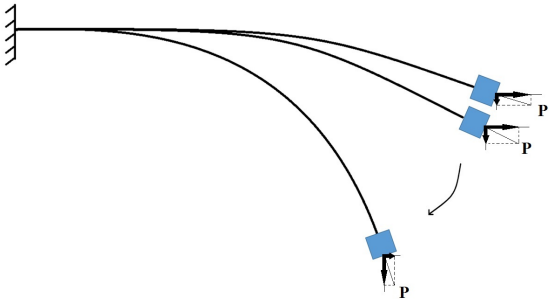

Figure 13. The great curvature created by the tensile follower force.

It was also verified that, when the tensile force reached its maximum limit, the ruler, besides presenting a great curvature, also presented a lateral torsion, generated by the combination between the weight of the motor/propeller assembly and the performance of this follower force.

As in the tests in which the rule was tested in the other positions (vertical and upside down), it was possible to observe in the horizontal position the difference of behavior of the structure when it is submitted to a follower force of compression and tension. While in the first the structure reached flutter instability, in the second it was possible to observe characteristics inherent in divergence instability. Figures 12 and 13 also show the decomposition of the applied force, which explains the difference of each behavior.

4.4 Tests with instrumentation

After the non-instrumentated tests, in which it was possible to qualitatively analyze the behavior of the structure when subjected to follower forces in different configurations, the tests were instrumented in order to try to capture data referring to these behaviors. The results obtained from these tests will be described in Section 5.

Instrumentated with accelerometers

The first attempt was to implement the ruler with accelerometers, so that it was possible to determine the transverse displacement of different points of the structure over time.

The tests were performed with three and four accelerometers distributed evenly along the 90 cm of the ruler, this time in a horizontal position. The ruler could not be tested with accelerometers in the vertical position due to the mass of the accelerometers, which caused the structure to buckle and collapse. The intention of this uniform distribution is to determine in which mode of vibration the structure was. Data was captured using an InfiniiVision© Mixed Signal Oscilloscope, model MSOX2024A.

For the test with four accelerometers, it was decided to balance the moment generated by the mass of the accelerometers. The accelerometers were positioned at an 11.25 cm (A1), 33.75 cm (B1), 56.25 cm (C1) and 78.75 (D1) distance to the set base of the ruler. These positions were obtained by subdividing the ruler into four quarters, each 22.5 cm long. The accelerometers were positioned in the middle of each quarter. Accelerometers A1 and D1 were glued to one side of the ruler, while accelerometers B1 and C1 were glued to the opposite side. In this way, theoretically, the moment generated in the set base from the mass of the accelerometers (and that would cause lateral torsion) would be null.

For the test with three accelerometers, this moment balance was not possible. However, similarly to the test with four accelerometers, the total length of the ruler was subdivided into three thirds, each 30 cm long. The accelerometers were positioned at 15.0 cm (A2), 45.0 cm (B2) and 75.0 cm (C2) distance to the set base of the ruler, as shown in Figure 14. Even though it was not possible to balance the moment as well as the test with four accelerometers, it was decided, as an attenuation attempt, to attach the accelerometers A2 and C2 on one side of the ruler and the B2 on the opposite side.

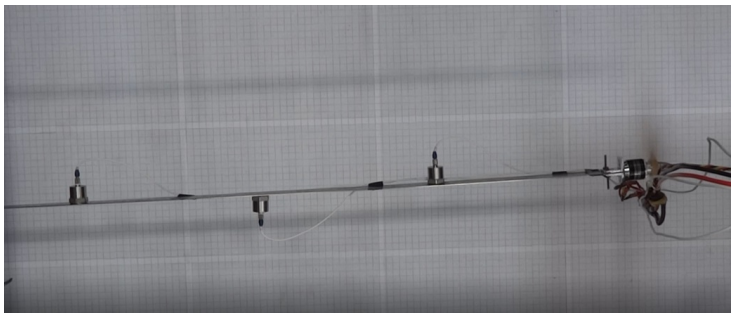

Figure 14. The horizontal in compression test, instrumented with accelerometers.

Instrumentated with LVDTs

The second attempt consisted in instrumenting the ruler with Linear Variable Differential Transformers (LVDTs). The intention, this time, was to avoid introducing additional masses to the structure (which occurred, for example, in the accelerometers instrumentation).

The ruler was placed on a flat metal plate, in which electromagnet bases were installed and to which the LVDTs were connected. A total of four LVDTs (one pair with a width of 20 mm and another with 50 mm) were used, which could capture the transverse displacement and the vibration frequency of a given point.

For this, each LVDT pair was positioned at the same longitudinal point of the ruler, but on the opposite side for balancing the system and avoiding undesired out-of-straightness (see Figure 15).

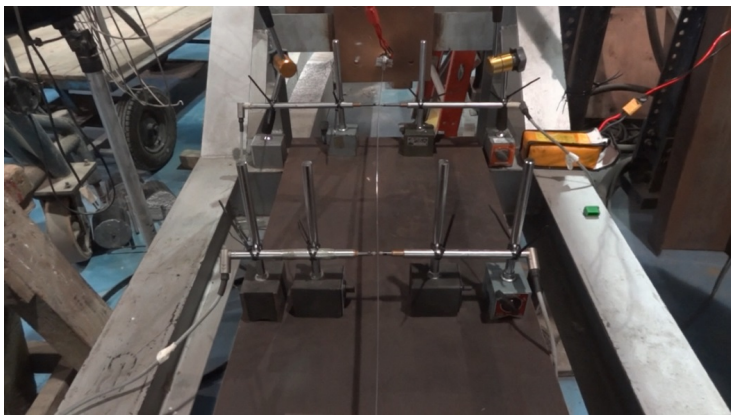

Figure 15. The test instrumented with LVDTs.

5 Results and discussion

In this section, the results of the instrumented tests and the respective interpretations will be presented.

5.1 Instrumentation with accelerometers

When the results, obtained by fixing accelerometers to the ruler, were analyzed, they were found to be unsatisfactory. It occurred that the masses of the accelerometers, added to the system, made it impossible for the structure to behave in the same way that it behaved when it was not instrumented. It is explained: as the mechanical energy generated by the motor remained the same and the system had a significant increase of mass, logically it would not be possible that the behavior remained the same. In order to obtain a similar behavior, in this case, it would be necessary to increase the energy generated by the motor.

It was also found that the equipment is extremely sensitive and somewhat incompatible with the noise caused by the proposed test, causing considerable interference in the obtained data.

Although it was possible to notice similarities between the curves generated by the tests with three and four accelerometers, as over time the trend of the curves is very similar on a large scale, it was observed, in a deeper analysis of the curves, a large degree of randomness in the behavior verified by each accelerometer. So, it was decided to use the moving average principle. So, the figures 16 and 17 were generated.

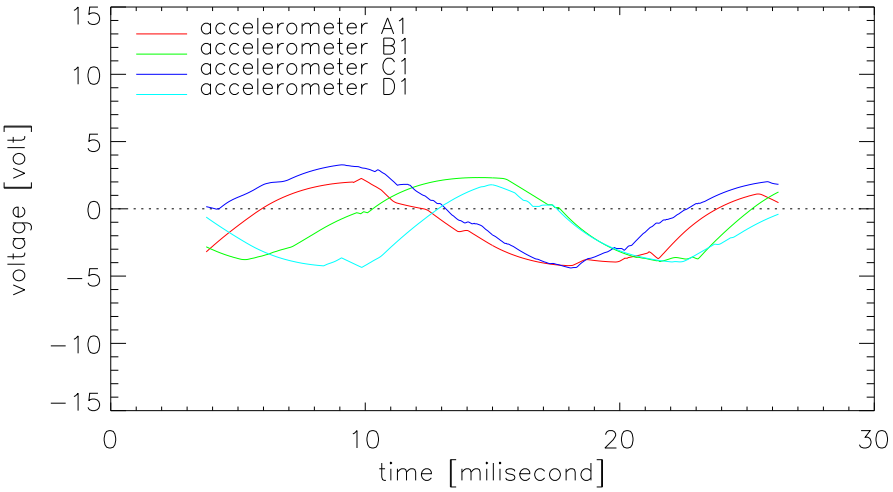

Figure 16. Test instrumented with four accelerometers, with noise attenuation.

As can be seen, when instrumented with four accelerometers, the displacement curves indicated that, although not possible to see with naked eye, the structure vibrated on second mode (see Table 2 and Figure 18). This inference is explained by the difference noted in the waves. The curves referring to the accelerometers A1 and C1 are in one phase, while those referring to B1 and D1 in another. However,

Table 2. Sign analysis for second mode.

Accelerometer	$A1$	$B1$	$C1$	$D1$
Side (left = +, right = −)	+	−	−	+
Position	+	+	−	−
Final data	+	−	+	−

when instrumented with three accelerometers, the displacement curves in the time domain leads to the belief that the structure vibrated on third mode (see Table 3 and Figure 19). This time, the inference is explained by the similarities noted in the waves (all the curves are in the same phase).

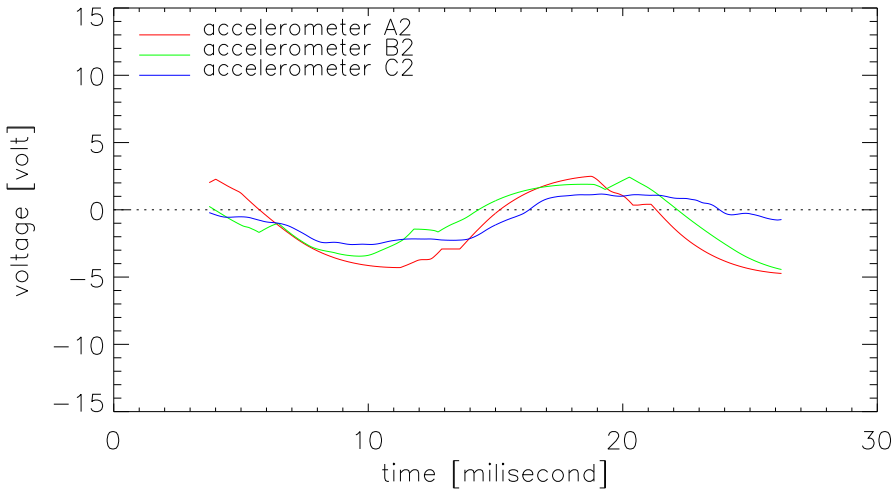

Figure 17. Test instrumented with three accelerometers, with noise attenuation.

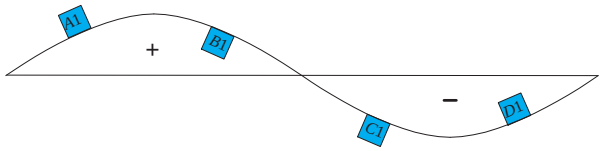

Figure 18. Four accelerometers' snapshot.

Table 3. Sign analysis for third mode.

Accelerometer	$A2$	$B2$	$C2$
Side (left = +, right = −)	+	−	+
Position	+	−	+
Final data	+	+	+

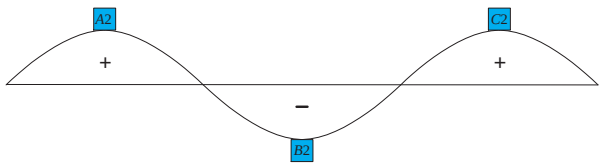

Figure 19. Three accelerometers' snapshot.

Both previous inferences are consistent because it is natural that, when removing the mass from an accelerometer (approximately 54 g), the structure attains higher modes of vibration.

Numerical modeling results

As the behavior of the structure was different from that observed in the compression test without instrumentation, it was decided to analyze the structure according to the modeling described in Section 3.

The mass of the motor/propeller assembly was considered equivalent to 90 g. The accelerometers were modeled considering the mass of 54 g. These data were obtained by weighing the components.

Free beam analysis

In the modeling considering the free beam (without the application of the tangential follower force), and disregarding the mass of the motor and the accelerometers, the vibration frequencies ω_1 and ω_2 were respectively equivalent to 0.20 and 1.26 rad/ms (31.83 and 200.54 Hz).

In Table 1, the values presented refer to the non-dimensional quantities $\omega_1^2 \frac{a\ell^4}{\pi^4}$ and $\omega_2^2 \frac{a\ell^4}{\pi^4}$.

So, if $\omega_1 = 0.20$ and $\omega_2 = 1.26$, the values presented in the table should be

$$\omega_1^2 \frac{a\ell^4}{\pi^4} = 0.20^2 \frac{\frac{0.00021}{210{,}000 \times 2.1577} 900^4}{\pi^4} = 0.125 \tag{27}$$

and

$$\omega_2^2 \frac{a\ell^4}{\pi^4} = 1.26^2 \frac{\frac{0.00021}{210{,}000 \times 2.1577} 900^4}{\pi^4} = 4.956. \tag{28}$$

Thus, it was concluded that the table presented by Timoshenko and Gere present a starting value (without the application of the follower force) different from that found in the modeling. This is, therefore, believed to be the cause of the disparity between Beck's and Timoshenko and Gere's P_{cr} values.

On the other hand, Weaver et al. [7] present the following table for determining the free beam vibration frequency.

Table 4. Values of $k\ell$ given by Weaver et al.

$k_1\ell$	$k_2\ell$	$k_3\ell$	$k_4\ell$	$k_5\ell$	$k_6\ell$
1.875	4.694	7.855	10.996	14.137	17.279

So,

$$k_1 = \frac{1.875}{\ell} = \frac{1.875}{900} = 0.002083 \text{ mm}^{-1} \tag{29}$$

and

$$k_2 = \frac{4.694}{\ell} = \frac{4.694}{900} = 0.005215 \text{ mm}^{-1}. \tag{30}$$

The following equation is also presented by Weaver et al.

$$\omega = k^2 \sqrt{\frac{EI}{\rho A}}, \tag{31}$$

where $\rho A = m$. So,

$$\omega_1 = k_1^2 \sqrt{\frac{EI}{m}} = 0.002083^2 \sqrt{\frac{210,000 \times 2.1577}{0.000210}} = 0.20 \text{ rad/ms} \tag{32}$$

and

$$\omega_2 = k_2^2 \sqrt{\frac{EI}{m}} = 0.005215^2 \sqrt{\frac{210,000 \times 2.1577}{0.000210}} = 1.26 \text{ rad/ms}. \tag{33}$$

Thus, it is possible to conclude that the values found by the vibration mode modeling for free beams were confirmed with the equations presented by Weaver et al. [7].

Next, the mass of the motor was included in the system. The masses were included in the numerical model using the complete shape functions (in other words, a consistent mass matrix is used for both the beam and the added masses). A load applied at a distance ℓ from the fixed end was considered. The vibration frequencies, ω_1 and ω_2, were, respectively, 0.12 and 0.97 rad/ms (19.10 and 154.38 Hz).

Finally, masses of accelerometers were included in the system. In this analysis, we considered the experiment with three accelerometers, positioned as described in Subsection 4.4. The vibration frequencies, ω_1 and ω_2, were, respectively, 0.10 and 0.76 rad/ms (15.92 and 120.96 Hz). So, the inclusion of the accelerometers did not cause a major change in the first mode vibration frequency and was therefore more impacting in the second mode value. This is due to the previous inclusion of the motor mass which significantly restricted the vibration in first mode, leaving the inclusion of the accelerometers, installed along the ruler, to increase the vibration restriction in the second mode.

The results from the free beam analysis are shown in Table 5.

Table 5. Free beam analysis.

Free beam			
parameter	beam	beam + motor	beam + motor + accelerometers
ω_1 [rad/ms]	0.20	0.12	0.10
ω_2 [rad/ms]	1.26	0.97	0.76

Compression analysis

The modeling of the beam, disregarding the mass of the motor and accelerometers, when subjected to a tangential compression follower force, resulted in a P_{cr} equivalent to 11.21 N and a vibration frequency ω equivalent to 0.63 rad/ms (100.27 Hz).

When the motor mass was included, the P_{cr} showed a reduction of approximately 20.0%, equivalent to 9.01 N. The vibration frequency ω was equivalent to 0.42 rad/ms (66.85 Hz).

Finally, by including the mass of the three accelerometers, the P_{cr} showed an increase, representing a smaller reduction, of approximately 16.8% of the original value (11.21 N), equal to 9.33 N. The vibration frequency ω, on the other hand, showed a reduction, equivalent to 0.35 rad/ms (55.70Hz). The values found (increase of P_{cr} and decrease of vibration frequency), therefore, corroborate with the change in the behavior of the structure that was observed in the compression test instrumented with accelerometers.

The results from the compression analysis are shown in Table 6.

5.2 Instrumentation with LVDTs

As mentioned previously, for this test, two pairs of LVDT's were used, one with 20 mm and the other with a 50 mm amplitude. Each pair was positioned at the same longitudinal point of the ruler, but on opposite sides.

Table 6. Compression analysis.

Compression			
parameter	beam	beam + motor	beam + motor + accelerometers
P_{cr} [N]	11.21	9.01	9.33
ω [rad/ms]	0.63	0.42	0.35

Since each LVDT has a spring (and hence an elastic coefficient k), in theory, positioning a pair of each side at one point would cause the force resulting from the one-way spring to compensate for the force resulting from the spring of the opposite side (assuming that the elastic coefficients of the springs of each pair are equivalent). This, in fact, occurred, but only in the initial position, before the motor was started, as shown in Figure 20. When the structure began to move, the springs acted together, generating a non-zero resultant force.

Each LVDT was initially pressed to half its full extent causing the spring to be partially compressed. For example, each LVDT whose amplitude was 20 mm was initially pressed up to 10 mm and positioned in contact with the ruler. Therefore, at the initial stage (before motor start), a given longitudinal point had two LVDTs, one on each side, pressed down to its half (10 mm). So, when the ruler moves to one side, the opposite side did not lose contact with the ruler. Therefore, the point instrumented with the pair of LVDTs of 20 mm of amplitude could move, at most, these 20 mm, being 10 mm for each side of the axis.

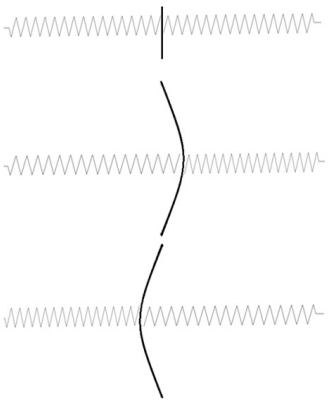

Figure 20. Non-zero resultant force.

This phenomenon caused the introduction of transverse displacement restraining points where the LVDTs were installed. Because of this, in this case, the ruler also did not have the same behavior when compared to the test without instrumentation.

With the purpose of attenuating this effect, tests were also performed using only a pair of LVDTs with 20mm course. Even so, the same effect was observed.

In Figure 21, it is observed that the pair of LVDTs positioned closer to the motor (therefore farther from the fixed end) had a considerably smaller transverse displacement than the fixed end nearest pair. Due to the displacements between the pairs of LVDTs having different magnitudes, it is possible to observe in the figure only the curves of the pair of greater magnitude, the others being close to zero.

On the other hand, in both figures (21 and 22) it is possible to observe that each pair of LVDTs behave in a mirrored way. It is also possible to observe that, before the motor is activated, the reading of each LVDT is null and, after the switch-off, the reading of each LVDT presents a non-null value. This is due to the fact that, after the motor is switched off, the final transverse position of a given point of the

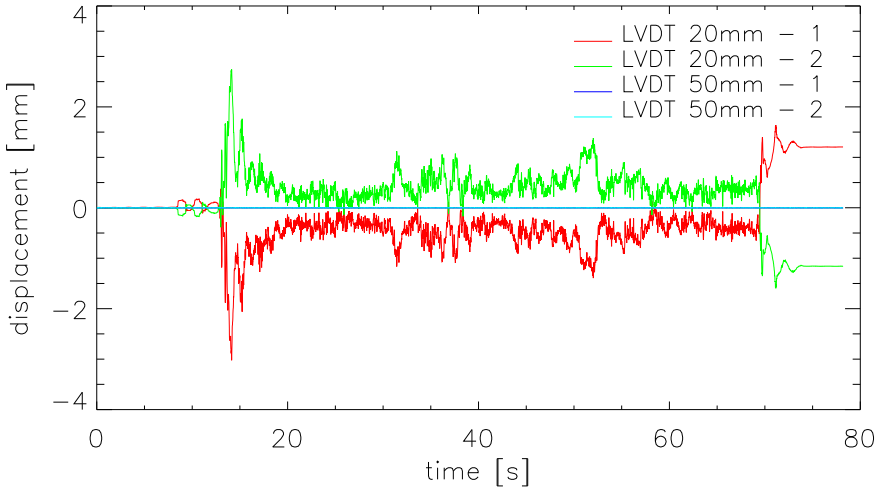

Figure 21. Test instrumented with two pairs of LVDTs.

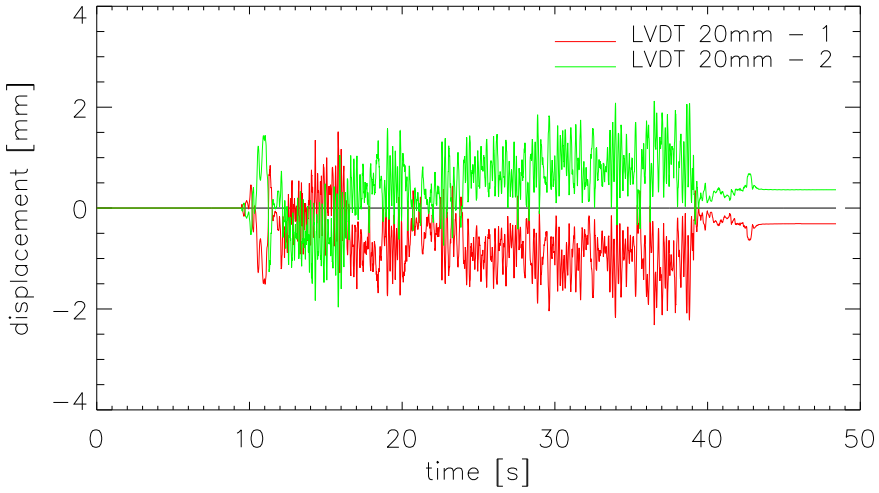

Figure 22. Test instrumented with one pair of LVDTs.

ruler is different from its initial position, resulting in a non-zero reading, since the spring in one LVDT will be more compressed than the spring in its counterpart.

6 Conclusions

Beck's Column is an idealized structure introduced in 1952 and has since divided researchers' opinions. Several recent studies, from the late 20th century and the early 21st century, have deepened the analysis of the behavior of this structure, and no consensus has yet been reached on the subject.

Although it is extremely difficult to create a beam-column subject to a tangential follower force, the structure created in this study was shown to be similar to Beck's Column. The brushless motor, fixed to the free end of the metallic ruler, made the force applied, at all times, tangential to the curvature of the ruler. This setup is an interesting alternative to the one with friction forces presented by Bigoni and Noselli [8].

In the analysis with the beam-column positioned vertically, it was possible to observe that the gravitational forces had considerable influence on the structure.

In the analysis of the beam-column positioned horizontally, the effects of gravity were reduced. It was therefore possible to clearly observe the differences in the behavior when the structure is subjected to compression and tensile tangential follower forces. When subjected to compression, the structure evidenced the occurrence of flutter, while when subject to tension the occurrence of divergence.

In an attempt to extract data, it was decided to add instrumentation to the test. When the test is performed with accelerometers fixed to the ruler, it was observed that the mass increase altered the behavior of the structure. This result is understood because, while the mechanical energy generated by the motor remained the same, there was an increase in the mass of the structure. A numerical modeling, presented in this research, corroborates this hypothesis.

When the test was performed with LVDTs by measuring the transverse displacement of certain points of the ruler, the stiffness of the LVDTs springs influenced the behavior of the structure. At the points where the LVDTs were positioned, the transverse displacement was compromised because the structure was freer to vibrate at the other points (which were not instrumented).

These two attempts to add instrumentation to the test, therefore, were unsatisfactory.

References

[1] Beck, M., 1952. Die knicklast des einseitig eingespannten, tangetial gredrückten stabes. *Zeitschrift für Angewandte Mathematik und Mechanik*, vol. 3, n. 3, pp. 225–228.

[2] Panokvo, Ya. G., G. I., 1965. *Stability and oscillations of elastic systems: paradoxes, fallacies, and new concepts*. Consultants Bureau.

[3] Timoshenko, S. P., G. J. M., 1961. *Theory of Elastic Stability*. Second Edition. McGraw-Hill Book Company, Inc.

[4] Koiter, W. T., 1996. Unrealistic follower forces. *Journal of Sound and Vibration*, vol. 194, n. 4, pp. 636–638.

[5] Silva, R. R., 2019. Instability of structures. class notes, Departamento de Engenharia Civil e Ambiental, PUC-Rio, Rio de Janeiro, Brazil.

[6] Bauchau, O. A., C. J. I., 2009. *Structural Analysis. Solid Mechanics and Its Applications*. First Edition. Springer Netherlands.

[7] Weaver, W., T. S. P. Y. D. H., 1990. *Vibration Problems in Engineering*. Fifth Edition. John Wiley & Sons.

[8] Bigoni, D., N. G., 2011. Experimental evidence of flutter and divergence instabilities induce by dry friction. *Journal of the Mechanics and Physics of Solids*, vol. 59, n. 10, pp. 2208–2226.